NUCL SCI TECH (2020) 31:86
https://doi.org/10.1007/s41365-020-00799-2

Digitalization of inverting filter shaping circuit for nuclear pulse signals

Huai-Qiang Zhang[1,2] · Hong-Tao Shi[2] · Zhuo-Dai Li[2] · Yu-Wen Li[2]

Received: 29 February 2020 / Revised: 22 July 2020 / Accepted: 24 July 2020 / Published online: 28 August 2020

Abstract In the design of filter shaping circuits for nuclear pulse signals, inverting filter shaping circuits perform better than non-inverting filter shaping circuits. Because these circuits facilitate changing the phase of a pulse signal, they are widely used in processing nuclear pulse signals. In this study, the transfer functions of four types of inverting filter shaping circuits, namely the common inverting filter shaping, improved inverting filter shaping, multiple feedback low-pass filter shaping, and third-order multiple feedback low-pass filter shaping, in the Laplacian domain, are derived. We establish the numerical recursive function models and digitalize the four circuits, obtain the transfer functions in the Z domain, and analyze the filter performance and amplitude–frequency response characteristics in the frequency domain. Based on the actual nuclear pulse signal of the Si-PIN detector, we realize four types of inverting digital shaping. The results show that under the same shaping parameters, the common inverting digital shaping has better amplitude extraction characteristics, the third-order multiple feedback low-pass digital shaping has better noise suppression performance, and the multiple feedback digital shaping takes into account both pulse amplitude extraction and noise suppression performance.

Keywords Nuclear pulse signal · Inverting filter shaping circuit · Digital shaping · Amplitude–frequency response

1 Introduction

When nuclear pulse signals are processed, the output nuclear pulse signal of the pre-amplified needs to be filtered and shaped to improve the signal-to-noise ratio (SNR) of the system and change the pulse shape for subsequent processing. Several studies have focused on analog non-inverting filter shaping circuits for nuclear pulse signals. Evariste et al. designed and developed a set of amplifier filter shaping circuits for Si (Li), CdZnTe and CsI detectors, which included a fourth-order integration stage and a differentiation stage [1]. Gan et al. designed a low-noise nuclear pulse signal processing system, in which CR-RC was used to realize filter shaping [2]. Gao et al. designed CR-RC and Sallen–Key circuits based on CdZnTe and Si-PIN detectors, which were used to shaped into quasi-Gaussian [3]. Zhang et al. developed a low-noise integrated circuit based on CR-RC^2, which exhibited excellent filtering effects [4]. The low-pass feedback terminal of the charge-sensitive preamplifier, based on RC low-pass feedback, was replaced by a junction field-effect transistor and an RC low-pass network for the high-resistance feedback resistor. The noise of the feedback terminal was considerably smaller than the thermal noise introduced by the high resistance feedback resistor [5]. In the work of Zeng et al. [6], a CR low-pass filter circuit was used to process the output signal of the high-purity germanium

This work was supported by the National Key R&D Project (No. 2017YFF0106503), National Natural Science Foundation of China (Nos. 11665001 and 41864007).

✉ Huai-Qiang Zhang
zhanghq821@163.com

[1] State Key Laboratory of Nuclear Resources and Environment, East China University of Technology, Nanchang 330013, China

[2] School of Nuclear Science and Engineering, East China University of Technology, Nanchang 330013, China

detector to filter out low-frequency interference. This circuit was equipped with a non-inverting follower and an adjustable gain amplifier circuit to amplify and filter the nuclear pulse signal. Wang et al. developed a compact 16-channel integrated charge-sensitive preamplifier to support the large-scale detector array used in modern nuclear physics experiments. A first-order RC filter circuit was employed to reduce the noise generated by the high voltage cable. Meanwhile, the resistor–capacitor feedback network formed a charge integrating and bleeding circuit that determined the energy sensitivity and pulse decay time [7]. The above circuits were designed and analyzed for their performance as analog non-inverting amplification filter shaping circuits for nuclear pulse signals.

We summarize the major works reporting the digital non-inverting filter shaping method of nuclear pulse signals as follows. Zhang et al. used the digital trapezoidal shaping method to process the simulated nuclear signal and the actual sampled nuclear signal to obtain the best digital shaping parameters [8]. Zhang et al. [9] derived the transfer function of the filter shaping circuit based on Sallen–Key in the Laplacian and Z domains and improved its numerical recursive function model at various values of resistance and capacitance. A comparative analysis of performance indicators, such as amplitude extraction and noise suppression, led to the optimal design model and filter shaping parameters. The CR-RC^m digital shaping method of nuclear pulse signal processing was implemented based on FPGA [10]. Zhou et al. derived the Sallen–Key numerical recursive function model using Kirchhoff's current law. This was also the earliest digital shaping processing of nuclear pulse signals in the temporal domain [11]. Zhou et al. [12] also used the results of earlier studies to improve the digital Sallen–Key recursive function model and introduce the amplitude adjustable parameter. The transfer function of the digital Sallen–Key circuit was derived in the Z domain and the nuclear pulse signal was convolved with the impulse response function. However, the result, when applied to the processing of the double-exponential nuclear pulse signal, did not improve the real-time performance. This limited the further use of this method [13]. Zhang et al. constructed a set of digital processing platforms for nuclear pulse signals based on MATLAB, which realized the digital shaping processing of simulated nuclear signals and actual sampled nuclear signals under different shaping methods and shaping parameters [14]. In a previous study, the quality factor and cut-off frequency of the digital Sallen–Key shaping method were introduced and simultaneously compared with the trapezoidal shaping results [15]. It was observed that digital Gaussian shaping based on the Sallen–Key method exhibited better noise suppression performance, which was beneficial for pulse amplitude extraction. In contrast, digital Gaussian shaping based on CR-RC^m had better counting rate characteristics, which aided pulse pile-up identification [16]. Zhang et al. studied the digitization of the pole-zero cancellation and Sallen–Key filter shaping circuits and obtained the numerical recursive function model and the amplitude–frequency response curve, respectively [17]. Liu et al. applied the CR-RC^m digital shaping method to the γ-spectrum measurement system and obtained the relationship between the shaping parameters and energy resolution [18]. Regadio et al. designed and developed a set of adjustable digital shapers for particle physics, which could adjust the shaping algorithm and shaping parameters according to actual requirements, and implemented the algorithm in FPGA [19]. Valentin used the unfolding-synthesis technique in digital pulse processing systems by digitizing analog signals according to the unfolding system and converting the nuclear signal into the desired pulse shapes [20]. The adaptive digital pulse shaping technique was investigated for real-time signal processing, and a digital Sallen–Key low-pass filter was implemented to enhance the SNR and reduce baseline drifting in this system [21].

In comparison with the non-inverting digital filter shaping method, the inverting digital shaping method exhibits a better SNR, which aids in pulse amplitude extraction under the same shaping parameters. The digital model functions of the inverting filter circuits, which were obtained using the numerical solution of differential equations, confirmed that the inverting digital shaping method exhibited better noise suppression performance [22]. However, the amplitude–frequency response was not analyzed, and hence, the numerical recursive function model of the serialized inverting filter shaping circuits was not analyzed and studied.

In this study, the digitalization of common inverting filter shaping circuits, improved inverting filter shaping circuits, multiple feedback low-pass filter shaping circuits and third-order multiple feedback low-pass filter shaping circuits is realized based on the preceding studies. The transfer function in the Laplacian domain, the amplitude–frequency response curve in the Z domain, and the numerical recursive function model are established. These are highly significant for the digital shaping processing of nuclear pulses and the optimal choice of parameters for nuclear pulse signal inverting filter shaping circuits.

2 Digitalization of inverting filter shaping circuits

Inverting filter shaping circuits for nuclear pulse signal processing include common inverting filter shaping circuits, improved inverting filter shaping circuits, multiple

feedback low-pass filter shaping circuits, and third-order multiple feedback low-pass filter shaping circuits.

2.1 Digitalization of the common inverting filter shaping circuit

The common inverting filter shaping circuit is composed of an operational amplifier (OPAMP) A, resistors R_1 and R_2 and capacitor C. The circuit is shown in Fig. 1.

As shown in Fig. 1, V_i and V_O are the input and output voltages, respectively, of the common inverting filter shaping circuit. The transfer function of the common inverting filter shaping circuit in the Laplacian domain is shown in Eq. (1).

$$H(s) = \frac{V_\mathrm{O}(s)}{V_\mathrm{i}(s)} = \frac{-\frac{1}{R_1 C}}{s + \frac{1}{R_2 C}} \tag{1}$$

When V_i is converted into x_i, V_O is converted into y_i, where $R_1 = R_2 = R$. According to differential numerical analysis, Eq. (1) leads to Eq. (2):

$$RC \cdot \frac{y_i - y_{i-1}}{\Delta t} + y_i = -x_i. \tag{2}$$

When x_i is converted into a sequence of numbers, $x[n]$, y_i is converted into a sequence of numbers, $y[n]$. Thus, Eq. (3) can be obtained:

$$y[n] = \frac{k \cdot y[n-1] - x[n]}{k+1}. \tag{3}$$

When $k = RC/\Delta t$ (Δt is sampling interval of ADC), the transfer function of the common inverting filter shaping circuit in the Z domain is as shown in Eq. (4):

$$H(z) = \frac{-1}{k + 1 - k \cdot z^{-1}}. \tag{4}$$

The frequency response function is:

$$H(e^{jw}) = \frac{-1}{k(1 - e^{-jw}) + 1}. \tag{5}$$

The modulus of Eq. (5) is shown in Eq. (6).

$$|H(e^{jw})| = \frac{1}{\sqrt{1 + 2k + 2k^2 - 2k(1+k) \cdot \cos(w)}}. \tag{6}$$

Equation (6) may be used to obtain the amplitude–frequency response curves.

2.2 Digitalization of the improved inverting filter shaping circuit

The improved inverting filter shaping circuit is composed of an OPAMP A, resistors R_1, R_2 and R_3 and capacitors C_1 and C_2. The corresponding circuit is shown in Fig. 2.

The transfer function in the Laplacian domain of the improved inverting filter shaping circuit shown in Fig. 2 is given by Eq. (7).

$$\begin{aligned} H(s) &= \frac{V_\mathrm{O}(s)}{V_\mathrm{i}(s)} \\ &= \frac{-\frac{1}{R_1 C_1} s - \frac{1}{R_1 R_2 C_1 C_2}}{s^2 + \left(\frac{1}{R_2 C_2} + \frac{1}{R_2 C_1} + \frac{1}{R_3 C_2}\right) s + \frac{1}{R_2 R_3 C_1 C_2}} \end{aligned} \tag{7}$$

When $R_1 = R_2 = R_3 = R$, $C_1 = C_2 = C$, according to the differential numerical analysis, Eq. (7) changes into Eq. (8).

$$\begin{aligned} (RC)^2 \cdot \frac{\frac{y_i - y_{i-1}}{\Delta t} - \frac{y_{i-1} - y_{i-2}}{\Delta t}}{\Delta t} + 3RC \cdot \frac{y_i - y_{i-1}}{\Delta t} + y_i \\ = -RC \cdot \frac{x_i - x_{i-1}}{\Delta t} - x_i \end{aligned} \tag{8}$$

Then, Eq. (9) can be obtained as

$$\begin{aligned} y[n] = &\frac{(2k^2 + 3k) \cdot y[n-1] - k^2 \cdot y[n-2]}{k^2 + 3k + 1} \\ &- \frac{-(k+1) \cdot x[n] - k \cdot x[n-1]}{k^2 + 3k + 1} \end{aligned} \tag{9}$$

When $k = RC/\Delta t$, the transfer function of the improved

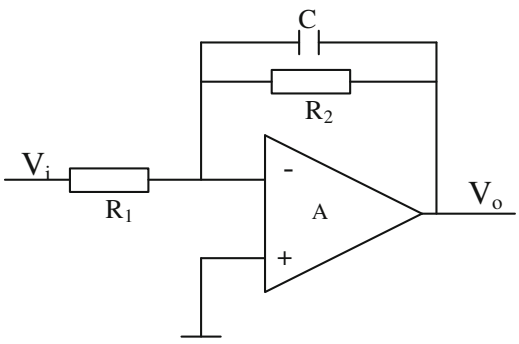

Fig. 1 Schematic diagram of the common inverting filter shaping circuit

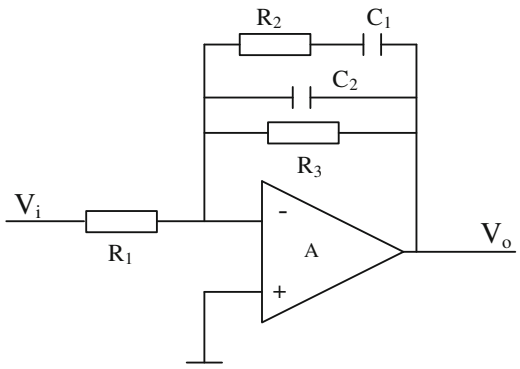

Fig. 2 Schematic diagram of the improved inverting filter shaping circuit

inverting filter shaping circuit in the Z domain is shown in Eq. (10).

$$H(z) = \frac{-k(1-z^{-1})-1}{k^2(1-z^{-1})^2 + 3k(1-z^{-1})+1} \tag{10}$$

The frequency response function is shown in Eq. (11):

$$H(e^{jw}) = \frac{-k(1-e^{-jw})-1}{k^2(1-e^{-jw})^2 + 3k(1-e^{-jw})+1} \tag{11}$$

The modulus of Eq. (11) is shown in Eq. (12).

$$\begin{aligned} |H(e^{jw})| &= \sqrt{\frac{1+2k+2k^2-2k(1+k)\cdot\cos(w)}{A-B\cdot\cos(w)+C\cdot\cos(2w)}} \\ A &= 1+6k+20k^2+18k^3+6k^4 \\ B &= 2k(3+11k+12k^2+4k^3) \\ C &= 2k^2(1+3k+k^2) \end{aligned} \tag{12}$$

The amplitude–frequency response curves can be obtained using Eq. (12).

2.3 Digitalization of the multiple feedback low-pass filter shaping circuit

The multiple feedback low-pass filter shaping circuit consists of an OPAMP A, resistors R_1, R_2 and R_3 and capacitors C_1 and C_2. The corresponding circuit is shown in Fig. 3.

In the Laplacian domain, the transfer function of the multiple feedback low-pass filter shaping circuit shown in Fig. 3 is given by Eq. (13).

$$\begin{aligned} H(s) &= \frac{V_O(s)}{V_i(s)} \\ &= \frac{-\frac{1}{R_1C_1R_2C_2}}{s^2 + s\frac{1}{C_1}\left(\frac{1}{R_1}+\frac{1}{R_2}+\frac{1}{R_3}\right)+\frac{1}{R_2C_1R_3C_2}} \end{aligned} \tag{13}$$

When $R_1 = R_2 = R_3 = R$, $C_1 = C_2 = C$, according to differential numerical analysis, Eq. (13) can be changed into Eq. (14).

$$\begin{aligned} &(RC)^2\cdot\frac{\frac{y_i-y_{i-1}}{\Delta t}-\frac{y_{i-1}-y_{i-2}}{\Delta t}}{\Delta t} \\ &+3RC\cdot\frac{y_i-y_{i-1}}{\Delta t}+y_i = -x_i \end{aligned} \tag{14}$$

Further derivation yields Eq. (15) as

$$y[n] = \frac{(2k^2+3k)\cdot y[n-1]-k^2\cdot y[n-2]-x[n]}{k^2+3k+1}. \tag{15}$$

When $k = RC/\Delta t$, the transfer function of the multiple feedback low-pass filter shaping circuit in the Z domain is shown in Eq. (16)

$$H(e^{jw}) = \frac{-1}{k^2(1-z^{-1})^2+3k(1-z^{-1})+1}. \tag{16}$$

The frequency response function is

$$H(e^{jw}) = \frac{-1}{k^2(1-e^{-jw})^2+3k(1-e^{-jw})+1}. \tag{17}$$

The modulus of Eq. (17) is given by Eq. (18).

$$\begin{aligned} |H(e^{jw})| &= \sqrt{\frac{1}{A-B\cdot\cos(w)+C\cdot\cos(2w)}} \\ A &= 1+6k+20k^2+18k^3+6k^4 \\ B &= 2k(3+11k+12k^2+4k^3) \\ C &= 2k^2(1+3k+k^2) \end{aligned} \tag{18}$$

The amplitude–frequency response curves can be obtained using Eq. (18).

2.4 Digitalization of the third-order multiple feedback low-pass filter shaping circuit

The third-order multiple feedback low-pass filter shaping circuit consists of an OPAMP A, resistors R_1, R_2, R_3 and R_4 and capacitors C_1, C_2 and C_3. The corresponding circuit is shown in Fig. 4.

The transfer function in the Laplacian domain of the third-order multiple feedback low-pass filter shaping circuit shown in Fig. 4 is given by Eq.(19).

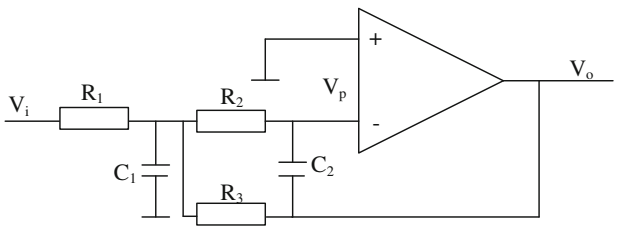

Fig. 3 Schematic diagram of the multiple feedback low-pass filter shaping circuit

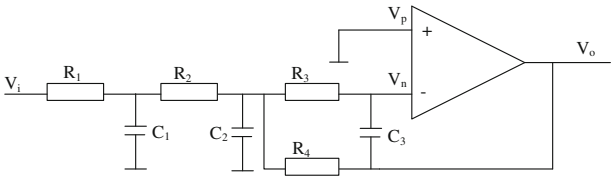

Fig. 4 Schematic diagram of the third-order multiple feedback low-pass filter shaping circuit

$$
\begin{aligned}
H(s) &= \frac{V_{\mathrm{O}}(s)}{V_{\mathrm{i}}(s)} \\
&= \frac{-\frac{1}{R_1R_2R_3C_1C_2C_3}}{s^3+s^2\left(\frac{1}{R_1C_1}+\frac{1}{R_2C_1}+\frac{1}{R_2C_2}+\frac{1}{R_3C_2}+\frac{1}{R_4C_2}\right)} \\
&\quad +\cdots s\left(\frac{1}{R_1R_2C_1C_2}+\frac{1}{R_1R_3C_1C_2}+\frac{1}{R_2R_3C_1C_2}\right) \\
&\quad +\cdots s\left(\frac{1}{R_2R_4C_1C_2}+\frac{1}{R_1R_4C_1C_2}+\frac{1}{R_3R_4C_2C_3}\right) \\
&\quad +\cdots \frac{R_1+R_2}{R_1R_2R_3R_4C_1C_2C_3}
\end{aligned}
\tag{19}
$$

When $R_1 = R_2 = R_3 = R_4 = R, C_1 = C_2 = C_3 = C$, Eq. (19) can be changed into Eq. (20) using differential numerical analysis.

$$
\begin{aligned}
&(RC)^3 \cdot \frac{\frac{\frac{y_i-y_{i-1}}{\Delta t}-\frac{y_{i-1}-y_{i-2}}{\Delta t}}{\Delta t}-\frac{\frac{y_{i-2}-y_{i-3}}{\Delta t}-\frac{y_{i-3}-y_{i-4}}{\Delta t}}{\Delta t}}{\Delta t} \\
&+\cdots 5(RC)^2 \cdot \frac{\frac{y_i-y_{i-1}}{\Delta t}-\frac{y_{i-1}-y_{i-2}}{\Delta t}}{\Delta t} \\
&+\cdots 6RC \cdot \frac{y_i-y_{i-1}}{\Delta t}+y_i = -x_i
\end{aligned}
\tag{20}
$$

Upon further derivation, Eq. (21) can be obtained.

$$
\begin{aligned}
y[n] &= \frac{(2k^3+10k^2+6k)\cdot y[n-1]-5k^2\cdot y[n-2]}{k^3+5k^2+6k+2} \\
&\quad -\cdots \frac{-2k^3\cdot y[n-3]-k^3\cdot y[n-4]-x[n]}{k^3+5k^2+6k+2}
\end{aligned}
\tag{21}
$$

When $k = RC/\Delta t$, the transfer function of the third-order multiple feedback low-pass filter shaping circuit in the Z domain is shown in Eq. (22).

$$
H(z) = \frac{-1}{k^3(1-z^{-1})^3(1+z^{-1})+5k^2(1-z^{-1})^2-6k(1-z^{-1})+2}
\tag{22}
$$

The frequency response function is shown in Eq. (23),

$$
H(z) = \frac{-1}{k^3(1-e^{-jw})^3(1+e^{-jw})+5k^2(1-e^{-jw})^2-6k(1-e^{-jw})+2}
\tag{23}
$$

and its modulus is given by Eq. (24).

$$
\begin{aligned}
|H(e^{jw})| &= \frac{1}{\sqrt{2\cdot(A-B\cdot\cos(w)-C\cdot\cos(2w)+D\cdot\cos(3w)-E\cdot\cos(4w))}} \\
A &= 5k^6+25k^5+57k^4-88k^3+46k^2-12k+2 \\
B &= 2k(2k^5+10k^4+41k^3-58k^2+28k-6) \\
C &= k^2(4k^4+20k^3-37k^2+30k-10) \\
D &= 4k^6+20k^5-18k^4+4k^3 \\
E &= k^6+5k^5-6k^4+2k^3
\end{aligned}
\tag{24}
$$

Equation (24) may be used to obtain the amplitude–frequency response curves.

2.5 Amplitude–frequency response curves of inverting filter shaping circuits

The amplitude–frequency response curves of common inverting filters at different shaping parameter values, according to Eq. (6), are shown in Fig. 5a. Figure 5b shows the amplitude–frequency response curves of the improved inverting filters at different shaping parameter values according to Eq. (12). The amplitude–frequency response curves of the multiple feedback low-pass filters at different shaping parameter values, according to Eq. (18), are shown in Fig. 5c. Similarly, Fig. 5d shows the amplitude–frequency response curves of third-order multiple feedback low-pass filters at different shaping parameter values according to Eq. (24).

Figure 5a shows that the common inverting filter shaping function model functions as a low-pass filter. When k is small, the amplitude–frequency response curve declines relatively slowly. As the value of k increases, the amplitude–frequency response curve declines faster. The closer the value of k is to zero, the smaller the cut-off frequency and the lower the noise suppression performance.

Figure 5b shows that the cut-off frequency of the improved inverting filter is lower than that of the common inverting filter. Thus, it performs better as a low-pass filter. Higher values of the shaping parameter k indicate better filtering performance.

From Fig. 5c, we observe that the multiple feedback low-pass filter shaping function model behaves as a low-pass filter. A comparison with the common inverting filter reveals similar behavior.

As shown in Fig. 5d, the cut-off frequency of the third-order multiple feedback low-pass filter is lower than that of

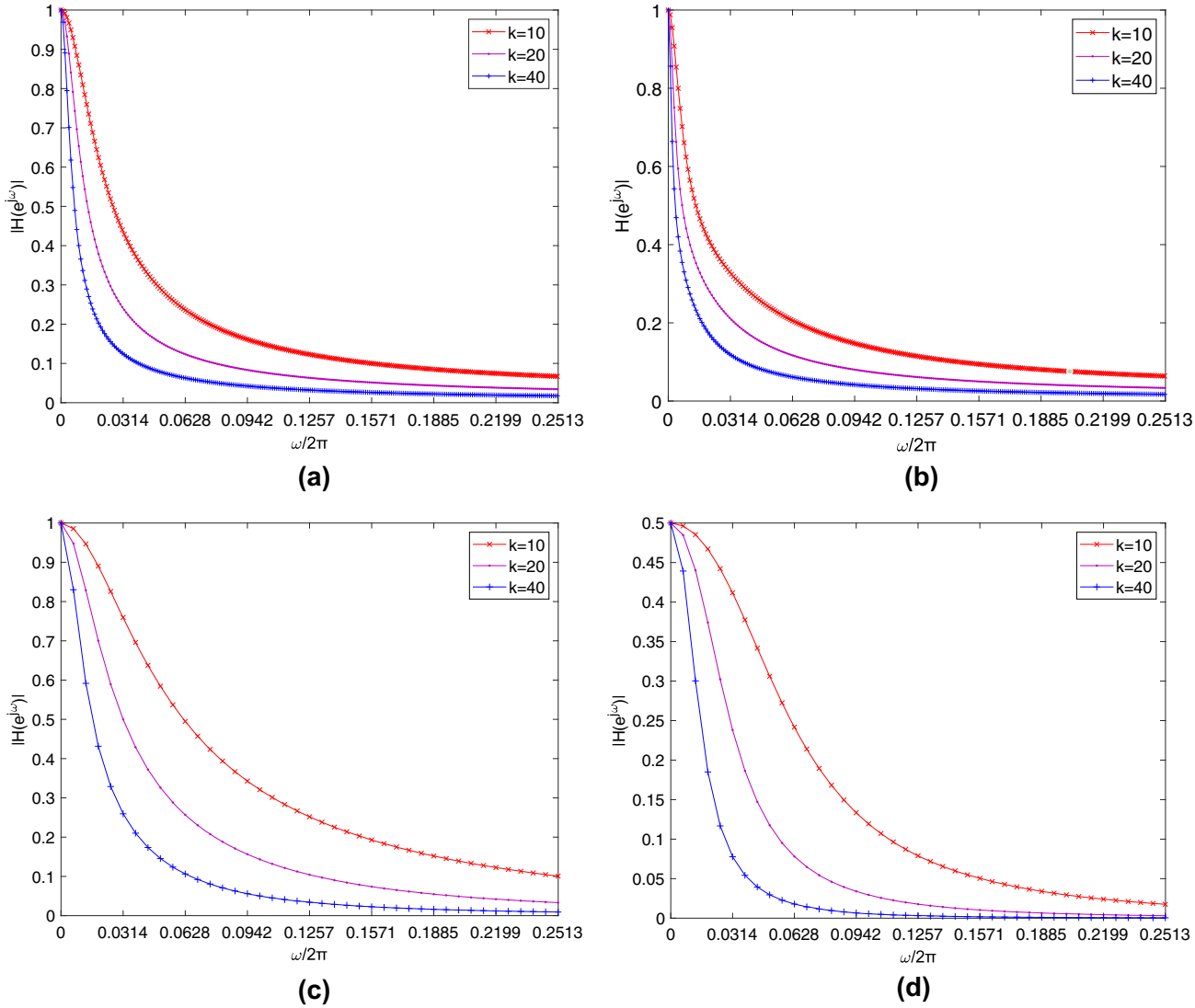

Fig. 5 (Color online) Frequency response curves at different shaping parameter values for the four types of filter shaping circuits. **a** Amplitude–frequency response curves of the common inverting filter shaping circuit; **b** Amplitude–frequency response curves of the improved inverting filter shaping circuit; **c** Amplitude–frequency response curves of the multiple feedback low-pass filter shaping circuit; **d** Amplitude–frequency response curves of the third-order multiple feedback low-pass filter shaping circuit

the multiple feedback low-pass filter, which indicates better low-pass filtering performance. The amplitude of this filter is the lowest among the four filters.

According to Fig. 5, a large RC value, i.e., a large value of k leads to a small cut-off frequency of the amplitude–frequency response curve and better noise suppression performance by digital filter shaping. This is beneficial for amplitude extraction and energy resolution of the system, but it simultaneously widens the digital Gaussian output, produces smaller peaks, and causes a slower time response, which are not conducive for pulse pile-up identification. This affects pulse counting rate the system. On the contrary, a smaller value of k implies a larger cut-off frequency, which defeats the purpose of filter shaping and affects the effective extraction and analysis of pulse amplitudes.

3 Comparative analysis of digital shaping results

The time constant of the front-end circuit of the signal output of the Si-PIN detector system is 10 μs. Digital shaping is performed using different shaping methods and shaping parameters at a sampling rate of 40 MHz. Equations (3), (9), (15), and (21) are used to implement the four types of inverting digital filter shaping processes for nuclear pulse signals.

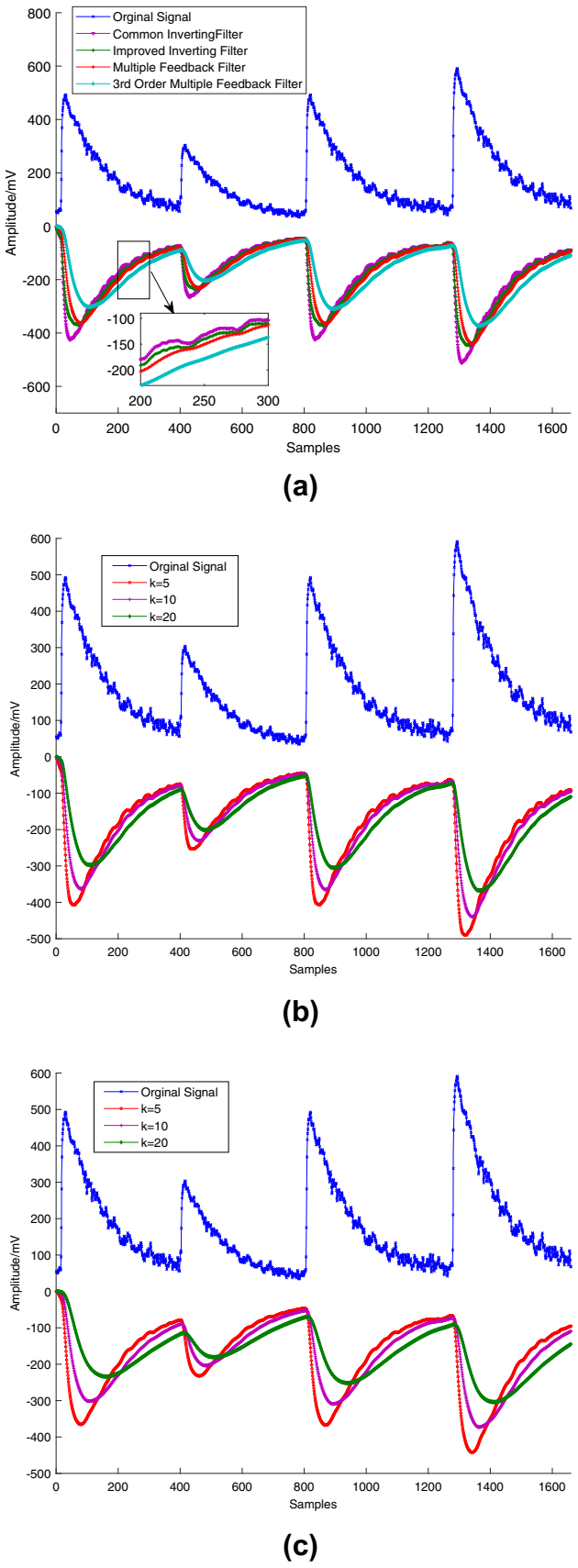

Fig. 6 (Color online) Shaping results of inverting digital filters. ▶ **a** Comparison of the digital shaping results; **b** Digital shaping outputs of the multi-feedback low-pass filter at different parameters; **c** Digital shaping outputs of the third-order multi-feedback low-pass filter at different parameters

3.1 Shaping results with inverting digital filter

The original signal is shaped using the same parameter value ($k = 10$). The numerical recursive modes of the common inverting filter shaping, improved inverting filter shaping, multiple feedback low-pass filter shaping, and third-order multiple feedback low-pass filter shaping are used to process nuclear pulse signals, and the results are shown in Fig. 6a. Considering the noise suppression performance and pulse amplitude extraction, the digital shaping outputs of the multi-feedback low-pass filter shaping circuit and the third-order multi-feedback low-pass filter shaping circuit at different shaping parameter values are selected for comparison and analysis. For the same signal, the digital shaping results of the above two methods when $k = 5, 10, 20$, are shown in Fig. 6b, c, respectively.

Figure 6a shows that at the same shaping parameter values, common inverting digital shaping output exhibits the largest amplitude, but the worst shaping symmetry and noise suppression performance. In comparison, improved inverting digital shaping performs better in terms of noise suppression and waveform symmetry. The third-order multi-feedback low-pass digital shaping output has the smallest pulse amplitude and the best noise suppression performance, whereas the multi-feedback low-pass digital shaping output exhibits the best noise suppression and pulse amplitude comprehensive performance.

Figure 6b indicates that the pulse amplitude, noise suppression, and peak position information of the multiple feedback digital shaping output differ at different shaping parameter values. As k increases, the noise suppression performance improves, the pulse amplitude becomes smaller, and the peak position of the shaping output pulse shifts to the right. The above conclusion is consistent with the theoretical analysis and the results of the amplitude–frequency response curve.

As shown in Fig. 6c, the digital shaping results of the third-order multi-feedback low-pass filter resemble those in Fig. 6b. However, in comparison with the multiple feedback digital shaping output, the third-order multiple feedback digital shaping output has an additional RC low-pass filter circuit at the front end, and therefore, under the same shaping parameter values, the third-order multiple feedback digital shaping output has better noise suppression performance. Additionally, the presence of the RC filter circuit lowers the amplitude of the output pulse amplitude

slightly. Therefore, in actual inverse digital shaping, the multiple feedback low-pass filter shaping circuit is capable of appropriately increasing the shaping parameter values to obtain a better SNR, and the third-order multiple feedback filter shaping circuit can appropriately reduce the shaping parameter value. Thus, the premise of ensuring better noise suppression leads to a higher SNR.

3.2 Performance analysis of digital shaping methods

To compare and analyze the outputs of inverting digital shaping under the same shaping parameter values and different methods, or the same shaping methods and different shaping parameter values, the amplitude, symmetry, and SNR after inverting digital shaping are quantitatively evaluated.

From Fig. 6, we observe that the output pulse amplitude of the inverting digital shaping has different degrees of attenuation for different shaping parameters. We quantitatively evaluate the amplitude attenuation index by using Eq. (25) to evaluate the amplitude attenuation.

$$d = \left(1 - \frac{A}{A_0}\right) \times 100\% \tag{25}$$

Here, A_0 and A are the pulse amplitudes before and after shaping, respectively, and d is the amplitude attenuation coefficient. A smaller d indicates lower pulse amplitude attenuation.

Equation (26) is used to quantitatively evaluate the symmetry of the digital shaping output.

$$\delta = \frac{\sum_{i=1}^{N}(x_{0-i} - x_{0+i})^2}{N} \tag{26}$$

Here, $i = 1, ...N$, is an integer, x_{0-i} is the ith point on the left side of the signal peak position, x_{0+i} is the ith point on the right side of the signal peak position, and N is the range of symmetry, i.e., the number of points. δ is used to indicate the degree of symmetry and a smaller δ implies better symmetry. For example, the δ of a Gaussian pulse is 0.

Equation (27) is used to quantitatively evaluate the SNR of the digital shaping output. A higher SNR indicates better noise suppression performance.

$$\mathrm{SNR} = \frac{V_{\max}}{\sqrt{\left(\sum_{i=1}^{N}(V_i - V_i')^2\right)\Big/N}} \tag{27}$$

Here, $V_{\max}$ is the maximum value of the output pulse amplitude, V_i is the pulse amplitude value corresponding to the ith point, V_i' is the pulse amplitude value of the ith point obtained using polynomial fitting, and N is the number of calculation points.

Table 1 shows the amplitude, symmetry, and SNR corresponding to Fig. 6. In particular, Table 1a–c correspond to Fig. 6a–c, respectively.

The amplitude attenuation is accurately estimated by using the third pulse in Fig. 6 for calculating the amplitude attenuation parameters.

Table 1a shows that the common inverting digital shaping method has the smallest amplitude attenuation index (14.15%), but its SNR (38.69) and symmetry (120.35) are the worst. In comparison, the third-order multiple feedback low-pass digital shaping method has the best SNR (52.30) and symmetry (0.61), but its amplitude attenuation index is poor (37.29%), while the multiple feedback low-pass digital shaping method exhibits the best synthesis performance.

As evident from Table 1b, for the multiple feedback low-pass digital shaping output, the amplitude attenuation index increases from 17.44 to 38.18%, the symmetry index parameter decreases from 13.09 to 0.018, and the SNR index is increased from 40.61 to 53.57, as k increases. The value of $k = 10$ is recommended to obtain the best comprehensive performance.

Table 1c shows that for the third-order multiple feedback low-pass digital shaping output, the amplitude attenuation index increases from 25.45 to 48.95%, the symmetry index parameter decreases from 2.67 to 0.0062, and the SNR index increases from 45.42 to 63.02 as k increases. After comprehensive consideration, $k = 5$ is found to be the best choice.

Table 1 Performance comparison of inverting digital filters

Shaping methods	d (%)	δ	SNR
(a) *Performance comparison of different shaping methods*			
Common inverting	14.15	120.35	38.69
Improved inverting	24.68	9.57	40.30
Multiple feedback	26.01	3.45	46.23
Third-order multiple	37.29	0.61	52.30
Shaping parameter	d (%)	δ	SNR
(b) *Performance comparison of the multiple feedback digital shaping method*			
$k = 5$	17.44	13.09	40.61
$k = 10$	26.01	3.45	46.23
$k = 20$	38.18	0.018	53.57
(c) *Performance comparison of the third-order multiple feedback digital shaping method*			
$k = 5$	25.45	2.67	45.42
$k = 10$	37.29	0.61	52.30
$k = 20$	48.95	0.0062	63.02

4 Conclusion

The digitalization of the common inverting filter shaping circuit, improved inverting filter shaping circuit, multiple feedback low-pass filter shaping circuit, and third-order multiple feedback low-pass filtering shaping circuits were achieved. The transfer functions of the four types of circuits in the Laplacian and Z domains were obtained. An analysis of the filter performance showed that all the four types of filter shaping circuits exhibited low-pass filter performance. The digital shaping model of the third-order multiple feedback low-pass filter is preferred in terms of noise suppression and waveform symmetry performance. In contrast, in terms of comprehensive performance of amplitude extraction, noise suppression, and waveform symmetry, the digital shaping model of the multiple feedback low-pass filter is preferred.

References

1. W.T. Evariste, S.U. Hong, Q. Yi et al., Design and simulation of Gaussian shaping amplifier made only with CMOS FET for FEE of particle detector. Nucl. Sci. Tech. **21**(5), 312–315 (2010). https://doi.org/10.13538/j.1001-8042/nst.21
2. B. Gan, T.C. Wei, W. Gao et al., Design and performances of a low-noise and radiation-hardened readout ASIC for CdZnTe detectors. J. Semicond. **37**(6), 065007 (2016). https://doi.org/10.1088/1674-4926/37/6/065007
3. W. Gao, S. Li, Y. Duan et al., Design and characterization of a low-noise front-end readout ASIC in 0.18 $-\mu$m CMOS technology for CZT/Si-PIN detectors. IEEE Trans. Nucl. Sci. **65**(5), 1203–1211 (2018). https://doi.org/10.1109/TNS.2018.2826070
4. M.M. Zhang, Z.J. Chen, Y.C. Zhang et al., Design and test results of a low-noise readout integrated circuit for high-energy particle detectors. Nucl. Sci. Tech. **21**(1), 44–48 (2010). https://doi.org/10.13538/j.1001-8042/nst.21.44-48
5. Y. Rong, G.Q. Zeng, L.Q. Ge et al., Design of charge sensitive preamplifier based on RC low pass feedback. Nucl. Tech. **42**(9), 090402 (2019). https://doi.org/10.11889/j.0253-3219.2019.hjs.42.090402. (in Chinese)
6. G.Q. Zeng, S. Qing, X.P. OuYang et al., Preliminary development of a new high efficiency and compact anti-compton spectrometer. Nucl. Tech. **42**(2), 020401 (2019). https://doi.org/10.11889/j.0253-3219.2019.hjs.42.020401. (in Chinese)
7. D.X. Wang, C.J. Lin, L. Yang et al., Compact 16-channel integrated charge-sensitive preamplifier module for silicon strip detectors. Nucl. Sci. Tech. **31**, 48 (2020). https://doi.org/10.1007/s41365-020-00755-0
8. H.Q. Zhang, Z.D. Li, B. Tang et al., Optimal parameter choice of CR-RC^m digital filter in nuclear pulse processing. Nucl. Sci. Tech. **30**, 108 (2019). https://doi.org/10.1007/s41365-019-0638-7
9. H.Q. Zhang, B. Tang, H.X. Wu et al., Study of Sallen–Key digital filters in nuclear pulse signal processing. Nucl. Sci. Tech. **30**, 145 (2019). https://doi.org/10.1007/s41365-019-0679-y
10. Y.Y. Liu, J.L. Zhang, L.F. Liu et al., Implementation of real-time digital CR-RC^m shaping filter on FPGA for gamma-ray spectroscopy. Nucl. Instrum. Methods Phys. Res. Sect. A **906**, 1–9 (2018)
11. J.B. Zhou, W. Zhou, J.R. Lei et al., Study of time-domain digital pulse shaping algorithms for nuclear signals. Nucl. Sci. Tech. **23**(3), 150–155 (2012). https://doi.org/10.13538/j.1001-8042/nst.23.150-155
12. J.B. Zhou, W. Zhou, X. Hong, Improvement of digital S-K filter and its application in nuclear signal processing. Nucl. Sci. Tech. **24**(6), 060401 (2013). https://doi.org/10.13538/j.1001-8042/nst.2013.06.020
13. Q. Ge, L.Q. Ge, H.W. Yuan et al., A new digital Gaussian pulse shaping algorithm based on bilinear transformation. Nucl. Sci. Tech. **26**(1), 010402 (2015). https://doi.org/10.13538/j.1001-8042/nst.26.010402
14. H.Q. Zhang, W.H. Lu, B. Tang, Digital shaping and performance analysis of nuclear pulse signal based on MATLAB. Nucl. Tech. **41**(10), 100401 (2018). https://doi.org/10.11889/j.0253-3219.2018.hjs.41.100401. (in Chinese)
15. X. Hong, S.J. Ni, J.B. Zhou et al., Simulation study on Gaussian pulse shaping algorithm. Nucl. Tech. **39**(11), 110403 (2016). https://doi.org/10.11889/j.0253-3219.2016.hjs.39.110403. (in Chinese)
16. Z.D. Li, H.Q. Zhang, J.Y. Liu et al., Implementation and analysis of Gaussian shaping method for digital nuclear pulse signal. Nucl. Tech. **42**(6), 060403 (2019). https://doi.org/10.11889/j.0253-3219.2019.hjs.42.060403. (in Chinese)
17. H.Q. Zhang, M.M. Yan, J.Y. Liu, Digitalization of filter shaping circuit for nuclear pulse signal. Nucl. Tech. **42**(7), 070402 (2019). https://doi.org/10.11889/j.0253-3219.2019.hjs.42.070402. (in Chinese)
18. Y.Y. Liu, J.L. Zhang, R. Zhou et al., Digitalization of CR-RC^m filter. Nucl. Tech. **40**(6), 44–48 (2017). https://doi.org/10.11889/j.0253-3219.2017.hjs.40.060403. (in Chinese)
19. A. Regadio, S. Sanchez-Prieto, M. Prieto et al., Implementation of a real-time adaptive digital shaping for nuclear spectroscopy. Nucl. Instrum. Methods Phys. Res. Sect. A **735**, 297–303 (2014). https://doi.org/10.1016/j.nima.2013.09.063
20. Valentin T. Jordanov, Unfolding-synthesis technique for digital pulse processing. Part 1: Unfolding. Nucl. Instrum. Methods Phys. Res. Sect. A **805**, 63–71 (2016)
21. S. Saxena, A.I. Hawari, Investigation of FPGA-based real-time adaptive digital pulse shaping for high-count-rate applications. IEEE Trans. Nucl. Sci. **64**(7), 1733–1738 (2017). https://doi.org/10.1109/TNS.2017.2692219
22. J. Zhou, J.B. Zhou, J.R. Lei et al., Simulation analysis of numerical model of inverting and noninverting amplifier filter circuit for nuclear signal in time domain. China Measur. Test **41**(9), 101–105 (2015). https://doi.org/10.11857/j.issn.1674-5124.2015.09.023. (in Chinese)